# Development of Improved Algorithms and Multiscale Modeling Capability with SUNTANS

Oliver B. Fringer
473 Via Ortega, Room 187
Dept. of Civil and Environmental Engineering
Stanford University
Stanford, CA 94305
phone: (650) 725-6878 fax: (650) 725-9720 email: fringer@stanford.edu

## LONG-TERM GOALS

The long-term goal is to develop a nonhydrostatic, parallel ocean simulation tool that is capable of simulating processes on a wide range of scales through use of accurate numerical methods and high-performance computational algorithms. The tool will be applied to study highly nonlinear internal waves in coastal domains to develop an improved understanding of mechanisms that govern their generation, propagation, and dissipation.

## OBJECTIVES

The primary objective is to enhance the capabilities of the SUNTANS model through development of algorithms to study multiscale processes in estuaries and the coastal ocean.  This involves development of 1) improved momentum and scalar advection on unstructured, staggered grids, 2) accurate and efficient algorithms for solution of the nonhydrostatic pressure, and 3) adaptive grid capabiliites with adaptive mesh refinement and model nesting.

## APPROACH

This work focuses on the continued development of SUNTANS (Stanford Unstructured Nonhydrostatic Terrain-following Adaptive Navier-Stokes Simulator), a free-surface, nonhydrostatic, unstructured-grid, parallel coastal ocean and estuary simulation tool that solves the Navier-Stokes equations under the Boussinesq approximation (Fringer et al.,2006). The formulation is based on the method outlined by Casulli and Walters (2000), in which the free-surface and vertical diffusion are discretized with the theta method which eliminates the Courant condition associated with fast free-surface waves and the elevated friction term associated with small vertical grid spacing at the free-surface and bottom boundary.  For flows with extensive wetting and drying, advection of momentum is accomplished with the semi-Lagrangian advection scheme (Wang et al. 2011a), which ensures stability in the presence of cells that fill and empty with the tides.  Scalar advection is accomplished semi-implicitly and continuity of volume and mass are guaranteed for the hydrostatic solver.  The theta method for the free surface yields a two-dimensional Poisson equation, and the nonhydrostatic

pressure is governed by a three-dimensional Poisson equation. These are both solved with the preconditioned conjugate gradient algorithm with Jacobi and block-Jacobi preconditioning, respectively. Because the nonhydrostatic component of SUNTANS is essentially a correction to the hydrostatic component, SUNTANS can be run seamlessly in nonhydrostatic or hydrostatic modes. SUNTANS is written in the C programming language, and the message-passing interface (MPI) is employed for use in a distributed-memory parallel computing environment. SUNTANS employs the generalized length scale approach to Reynolds-averaged turbulence modeling (Wang et al. 2011b). The SUNTANS grid employs z-levels in the vertical and is unstructured in plan, which enables the resolution of complex coastlines and topographic features. Unstructured grids also enable the use of high grid resolution in regions of interest while coarsening the grid in regions where grid resolution is not required, thereby significantly reducing computational overhead.

## WORK COMPLETED

We completed the development of a nonhydrostatic isopycnal-coordinate model (Vitousek and Fringer 2014) and here present results of the test cases from that work (that were not reported in last year's annual report). Follow-on work as part of the FLEAT and NOPP DRIs will focus on implementing the isopycnal-coordinate model into the SUNTANS modeling framework. We have also performed large-eddy simulations of breaking internal waves on slopes and computed the associated cross-shelf transport. Although these simulations do not employ the SUNTANS model, it is our hope that the SUNTANS model will eventually have this capability.

## RESULTS

*Nonhydrostatic isopycnal-coordinate ocean model*

We completed a manuscript reporting the formulation and testing of a nonhydrostatic isopycnal coordinate ocean model (Vitousek and Fringer 2014), which to our knowledge represents the first of its kind. While numerous ocean models are written in isopycnal coordinates (most notably MICOM/HYCOM; Bleck et al., 1992; Bleck, 2002), our model is unique because it solves for the nonhydrostatic pressure. This enables us to compute nonhydrostatic internal solitary waves at a fraction of the computational cost of traditional z-coordinate models (e.g. Zhang et al. 2011) because the number of vertical coordinates can be reduced from $O(100)$ to $O(1)$ while still resolving a bulk of the internal wave energetics. Below we report on two test cases that highlight the features of the model. More detail on these test cases can be found in the paper by Vitousek and Fringer (2014).

Formation of internal solitary waves in a laboratory experiment: This test case compares the formation of an internal solitary-like wave train using the isopycnal-coordinate model to the laboratory experiments in Horn et al. (2001). The laboratory experiments investigate the formation of solitary waves in an approximately two-layer density profile with a pycnocline thickness of 0.01 m in an enclosed tank of depth 0.29 m and length 6 m. The internal interface is initialized with a linear tilt with a wave amplitude given by [0.01305, 0.0261,0.03915, 0.0522, 0.0783] m. The model of the laboratory experiments is run with 2 layers and 256 horizontal grid points and with a slightly lower density difference than the lab experiment because the finite-thickness pycnocline in the laboratory experiment reduces the wave speed slightly when compared to the two-layer model configuration. A drag coefficient Cd=0.0175 is employed, and the horizontal and vertical eddy-viscosities are equal and

given by $10^{-6}$ m$^2$ s$^{-1}$. These parameters are chosen to fit the amplitude of the solitary waves formed during the laboratory experiment. Figure 1 shows the results of the model-predicted time series of the interface displacements (located at the center of the tank) compared to the laboratory experiments of Horn et al. (2001). Agreement between the model and the laboratory experiments is excellent for the first half of the experiment (t < 200 s). However, for the second half of the experiments there is some mismatch in the phase and amplitude of the waves. Over the course of a laboratory experiment Horn et al. (2001) reported ''a gradual thickening of the density interface over the set, typically from approximately 1 cm-2 cm''. The finite-thickness interface and thickening are partly responsible for the mismatch with the model (which has a sharp interface and no interface thickening). Additionally, the model appears to form slightly wider solitary waves than the laboratory experiment. This indicates that the dispersive properties of the waves are not captured exactly in the model because of the two-layer approximation. Overall, however, the model adequately captures the formation of solitary waves in the laboratory experiment.
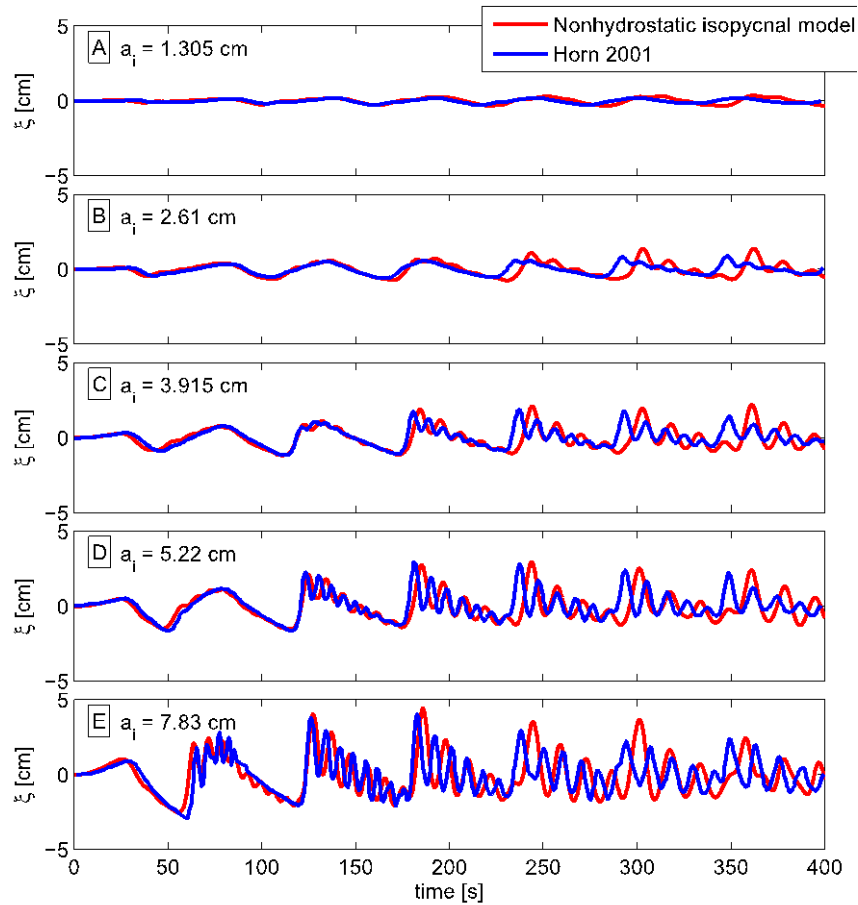


*Figure 1: Comparison of nonhydrostatic model-predicted and measured interface displacement time series at the middle of the tank from the experiments of Horn et al. (2001).*

Nonhydrostatic internal wave generation over a Gaussian ridge: Here we simulate the generation of internal tides over Gaussian ridge topography following the paper by Buijsman et al. (2010). The model is run with bathymetry that approximates the eastern ridge of the Luzon Strait with a height of 2600 m in a depth of 3000 m, as shown in Figure 2. This domain is 800 km long, and 1750 grid points

are used in the horizontal, which ensures that leading-order nonhydrostatic effects are resolved (Vitousek and Fringer 2011). The boundaries are forced with barotropic currents oscillating at the M2 tidal frequency and with a magnitude of 0.134 m s$^{-1}$. The initial 2- and 10-layer configurations are set to best match the weakly nonlinear and nonhydrostatic behavior of solitary waves in the stratification of Buijsman et al. (2010), which is representative of the South China Sea. The still-water isopycnal depths in the 10-layer model are set to z=0, 50, 100, 250, 460, 750, 1000, 1500, 2000, 2500, 3000 m with density values computed at the vertical center of each layer. The still-water internal interface for the 2-layer model is set to 460 m and the upper- and lower-layer densities are set to match the mode-1 wave speed of the 10-layer model. A horizontal eddy-viscosity of 100 m$^2$ s$^{-1}$ and a vertical eddy-viscosity of 10$^{-4}$ m$^2$ s$^{-1}$ are used to characterize unresolved mixing of momentum due to turbulence in the presence of internal waves, along with a bottom drag coefficient of Cd=0.0025.

Figure 3 compares the generation and evolution of internal solitary waves using 2 and 10 layers. Although both models form trains of nonlinear internal solitary-like waves with nearly identical wave speeds, the amplitude, length scales, and number of solitary waves differ between the models. The two-layer model only supports first-mode waves, whereas the 10-layer model supports higher modes. Consequently barotropic-to-baroclinic conversion in the 2-layer model is restricted to the first baroclinic mode, whereas energy is converted to higher-mode waves in the 10-layer model. This results in larger amplitude solitary waves in the 2-layer model relative to the 10-layer model. Additionally, the solitary wave widths in the 2-layer model are slightly larger than those in the 10-layer model due to unresolved nonhydrostatic dispersion in the 2-layer model.
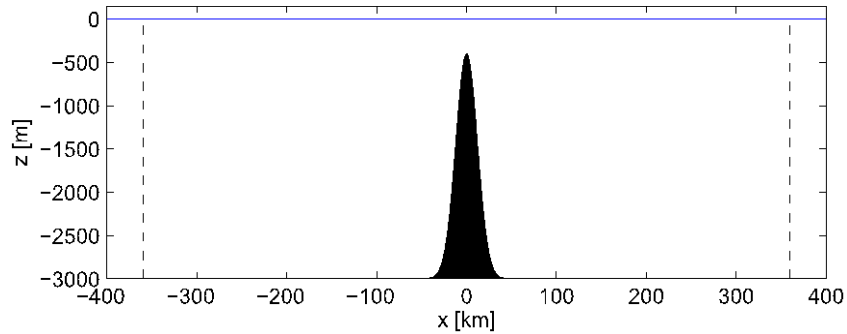


*Figure 2: Model domain and bathymetry used in the South China Sea case following Buijsman et al. (2010). The black filled area represents the bathymetry, the blue line represents the free surface, and the black dashed lines represent the locations of the sponge layers.*
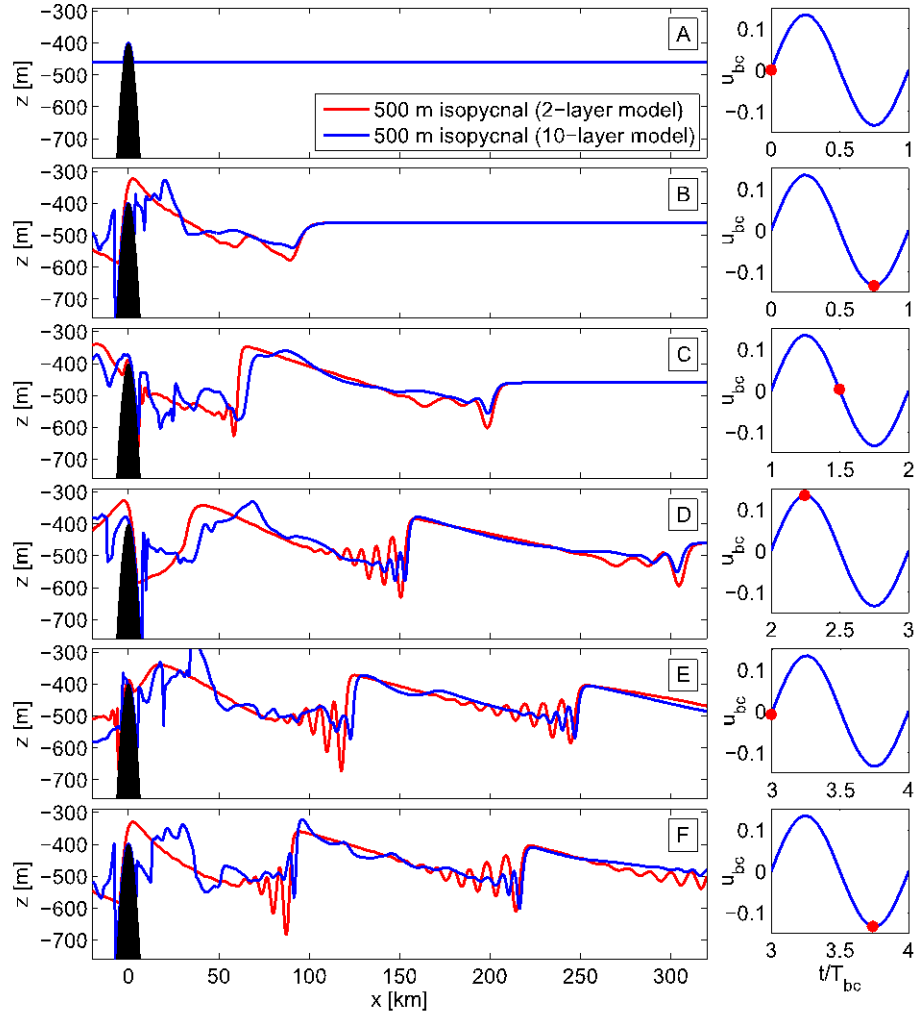
4

**Figure 3: Comparison of internal wave generation in the nonhydrostatic 2-layer (red) and 10-layer (blue) models at time intervals indicated by the red dot in the barotropic current time series in the panels in the right column.**

*Transport by breaking internal waves on slopes*

Using the code of Cui (1999), Arthur and Fringer (2014) performed three-dimensional DNS of breaking solitary-like internal waves on slopes to examine the energetics and mixing as a function of internal wave steepness and bathymetric steepness. Here we report on the results of transport by breaking internal waves computed with this same setup. Figure 4 shows snapshots in time of a plume of particles initially located where the pycnocline intersects the slope. As the wave begins to interact with the slope, particles are transported offshore in the lower layer and slightly onshore in the upper layer (Figure 4a-c). After the wave breaks, the upslope surge of dense fluid transports particles onshore. Upper-layer fluid is directed up and over the nose of the upslope surge, carrying a thin layer of particles offshore along the pycnocline (Figure 4d-e). Once the surge reaches its maximum upslope location, the relaxation of dense fluid transports particles back downslope (Figure 4f). When the jet detaches from the slope as an intrusion, particles are transported further offshore along the pycnocline (Figure 4f-i).

Over the course of the breaking event, onshore transport occurs along the bottom within the upslope surge of dense fluid. Offshore transport occurs along the pycnocline, initially due to flow over the nose of the upslope surge, and ultimately due to the offshore intrusion of intermediate density fluid. Above the pycnocline, there is minimal onshore transport that increases with depth. The shape of the plume at the end of the breaking event resembles the plume in the numerical dye study of Nakayama and Imberger (2010). Their study examined the cumulative effect of multiple periodic internal waves breaking on a slope, as opposed to the single wave of depression considered here.
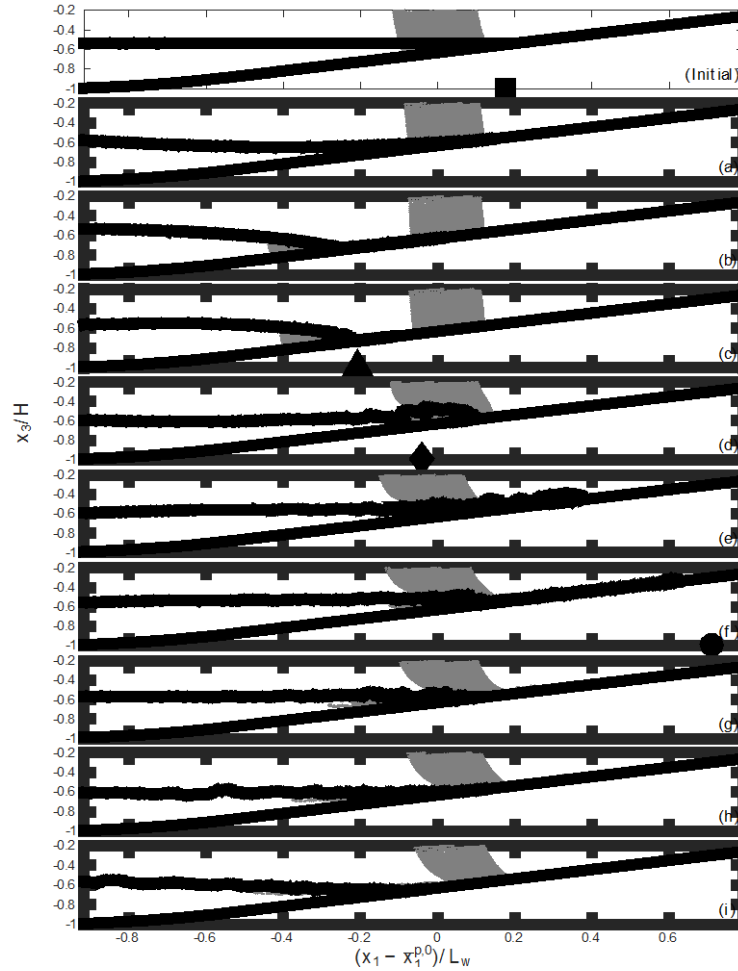


*Figure 4: Snapshots in time of a plume of particles for a breaking internal wave. The cross-shore position is presented relative to the initial mean position of the plume $\overline{x}_1^{p,0}$ and normalized by the solitary wave length $L_w$. The pycnocline is shown in black, while the top panel (labeled "Initial") shows the initial particle plume.*

The layer of particles transported offshore along the pycnocline by the breaking wave in Figure 4 resembles an intermediate nepheloid layer (INL; McPhee-Shaw et al. 2004, McPhee-Shaw 2006, Cheriton et al. 2014). If we define the INL as the group of particles within the density isosurfaces comprising the pycnocline, then the simulations can be used to determine the initial location of these particles. Figure 5 shows the INL formed at the end of the breaking event depicted in Figure 4, along with the location of the particles that comprise the INL prior to the breaking event. This figure shows

that mixing by the breaking internal wave causes particles to be entrained from above and below the pycnocline into the INL. In this particular case, 92% of the particles that comprise the INL originate outside of the pycnocline.
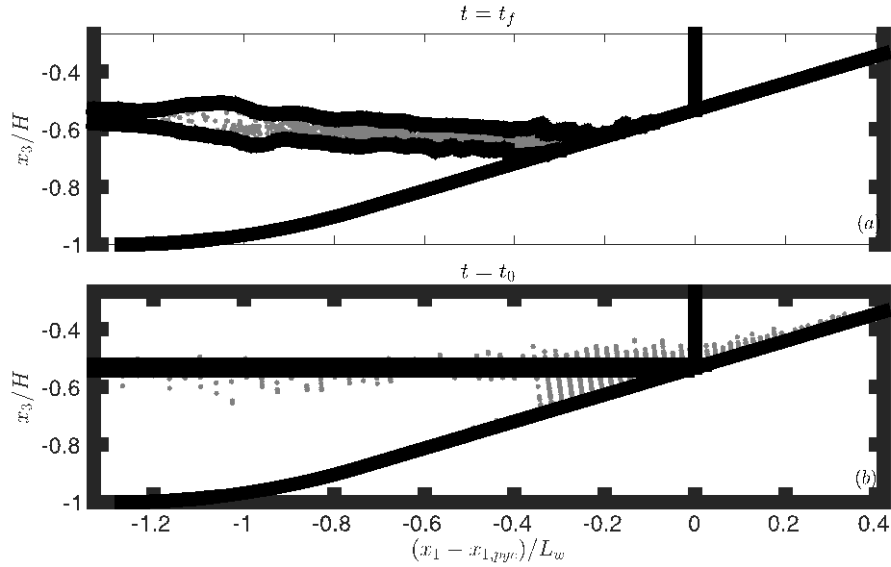


***Figure 5: Particles that make up the intermediate nepheloid layer for the breaking wave shown in Figure 4. (a) Shows the final positions of the particles within the INL at the end of the breaking event (time t = t_f), while (b) shows their initial positions (time t = t_0). Each plot shows density isosurfaces that make up the pycnocline as well as a vertical line at the cross-shore position x_{1,pyc} of the intersection of the initial pycnocline and the slope.***

The lateral turbulent velocities induced by breaking in the three-dimensional simulations lead to lateral transport of particles, as shown in Figure 6. Before turbulence develops, lateral transport occurs only due to a random walk based on the molecular diffusivity. However, after breaking, the flow becomes turbulent and lateral transport occurs at a faster rate. This increased lateral spreading is evident during the upslope surge (Figure 6e), and continues for the rest of the breaking event (Figure 6f-g). Most lateral transport appears to occur during the downslope flow of dense fluid after the upslope surge and the resulting intrusion of intermediate density fluid along the interface. Note that in Figure 6, particles are plotted outside of the lateral boundaries of the computational domain. This is because lateral particle positions were adjusted to account for periodic boundary crossings by adding or subtracting the width of the domain.
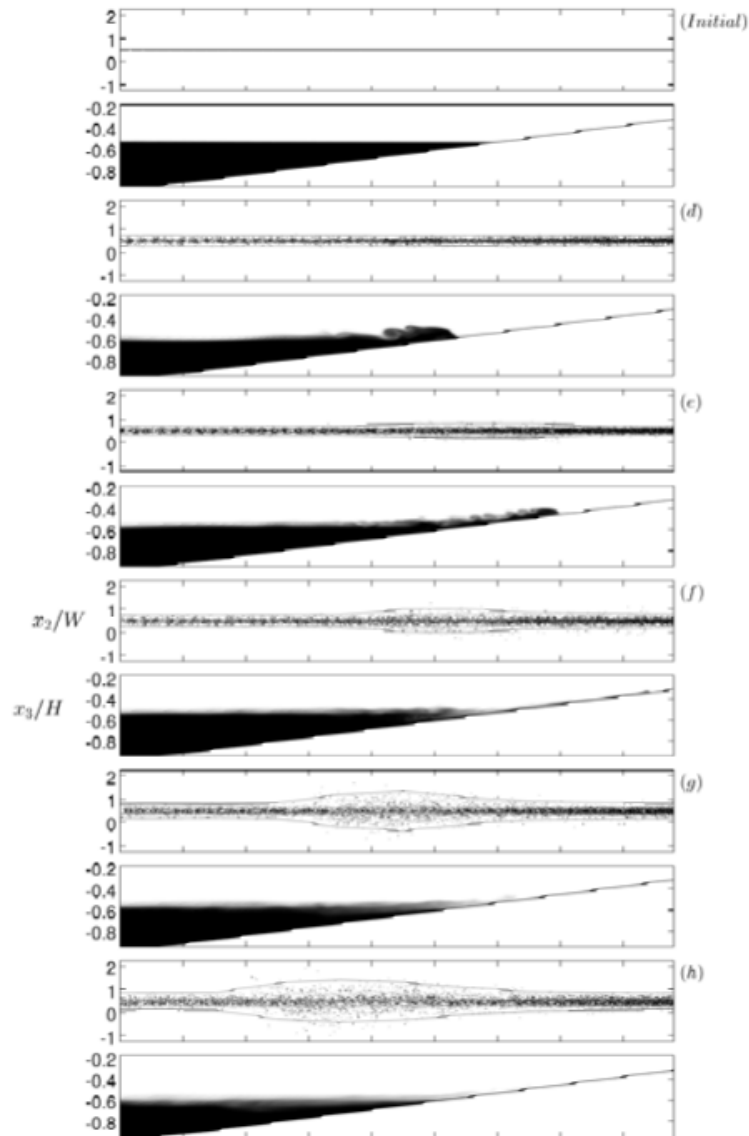
*Figure 6: Lateral transport of particles for a breaking internal wave. Each panel shows a top view ($x_1$-$x_2$) of all particles. For clarity, particles are shown to extend beyond the lateral boundaries of the domain owing to lateral periodicity. Also included are lines representing three standard deviations of the lateral particle positions, which indicate the lateral boundaries of the particle plume. Labels d-g correspond to the time snapshots shown in Figure 4.*

## IMPACT/APPLICATIONS

High-resolution simulations using nonhydrostatic models like SUNTANS are crucial for understanding multiscale processes that are unresolved, and hence parameterized, in larger-scale ocean models.

# REFERENCES

Arthur, R. S., and O. B. Fringer, 2014, The dynamics of breaking internal solitary waves on slopes, J. Fluid Mech., 761, 360-398.

Bleck, R., Rooth, C., Hu, D., Smith, L., 1992. Salinity-driven thermocline transients in a wind-and thermohaline-forced isopycnic coordinate model of the North Atlantic. J. Phys. Oceanogr. 22, 1486–1505.

Bleck, R., 2002. An oceanic general circulation model framed in hybrid isopycnic-Cartesian coordinates. Ocean Modell. 4, 55–88.

Buijsman, M.C., Kanarska, Y., McWilliams, J.C., 2010. On the generation and evolution of nonlinear internal waves in the South China Sea. J. Geophys. Res., 115.

Casulli, V. and R.A. Walters, 2000, An unstructured, three-dimensional model based on the shallow water equations, International Journal for Numerical Methods in Fluids, 32, 331-348.

Cheriton, O. M., McPhee-Shaw, E. E., Shaw, W. J., Stanton, T. P., Bellingham, J. G. and Storlazzi, C. D. 2014 Suspended particulate layers and internal waves over the southern monterey bay continental shelf: An important control on shelf mud belts? J. Geophys. Res. 119 (1), 428–444.

Cui, A. 1999 On the parallel computation of turbulent rotating stratified flows. PhD thesis, Stanford University.

Fringer, O. B., M. Gerritsen, and R. L. Street, 2006, An unstructured-grid, finite-volume, nonhydrostatic, parallel coastal ocean simulator. Ocean Modelling 14.3 (2006), 139-173.

Horn, D., Imberger, J., Ivey, G., 2001, The degeneration of large-scale interfacial gravity waves in lakes, J. Fluid Mech. 434, 181–207.

McPhee-Shaw, E. E. and Kunze, E. 2002 Boundary layer intrusions from a sloping bottom: A mechanism for generating intermediate nepheloid layers. J. Geophys. Res. 107 (C6), 1–16.

McPhee-Shaw, E. E., Sternberg, R. W., Mullenbach, B. & Ogston, A. S. 2004 Observations of intermediate nepheloid layers on the northern california continental margin. Cont. Shelf Res. 24 (6), 693–720.

Nakayama, K. and Imberger, J. 2010 Residual circulation due to internal waves shoaling on a slope. Limnol. Oceanogr. 55 (3), 1009–1023.

Vitousek, S., and O. B. Fringer, 2014, A nonhydrostatic, isopycnal-coordinate ocean model for internal waves, Ocean Modelling, 83, 118-144.

Wang, B., Zhao, G., and Fringer, O. B., 2011a, Reconstruction of vector fields for semi-Lagrangian advection on unstructured, staggered grids, Ocean Modelling, 40 (1), 52-71.

Wang, B., Giddings, S. N., Fringer, O. B., Gross, E.S., Fong, D. A., and Monismith, S. G., 2011b, Modeling and understanding turbulent mixing in a macrotidal salt wedge estuary, J. Geophys. Res., 116, C02036.

## PUBLICATIONS

R. S. Arthur and O. B. Fringer, 2015, "Transport by breaking internal waves on slopes", (poster/talk), Gordon Research Conference on Coastal Ocean Modeling, June 7-12, Biddeford, ME.

R. S. Arthur and O. B. Fringer, 2015, "Turbulent mixing and transport by breaking internal solitary waves on slopes" (talk), EUROMECH Colloquium 567: Turbulent mixing in stratified flows. March 22-25. Cambridge, UK.

R. S. Arthur and O. B. Fringer, 2014, "Turbulent dynamics of breaking internal gravity waves on slopes", (talk). 67th Annual Meeting of the APS Division of Fluid Dynamics. November 23-25, 2014. San Francisco, CA.

O. B. Fringer and R. S. Arthur, 2015, "Direct numerical simulation of transport and mixing in breaking internal waves on slopes" (invited talk), 13th US National Congress on Computational Mechanics, July 26-30, San Diego, CA.